ACS Catalysis

Research Article

Cite This: ACS Catal. 2018, 8, 6375−6387

pubs.acs.org/acscatalysis

Effects of Catalyst Model and High Adsorbate Coverages in ab Initio Studies of Alkane Hydrogenolysis

Abdulrahman Almithn and David Hibbitts*

Department of Chemical Engineering, University of Florida, Gainesville, Florida 32611, United States

Supporting Information

ABSTRACT: Bare, low-index periodic surface models are typically used to examine metal-catalyzed reactions in density functional theory (DFT) studies, and these most closely resemble low-pressure surface science reactions and catalyzed reactions that occur on large terraces that prevail on large (>5 nm) supported nanoparticles. Many catalytic reactions, however, occur near conditions at which catalytic surfaces are saturated by one or more adsorbed intermediates, leading to strong coadsorbate interactions and surface reconstruction leading to increased curvature. Alkane hydrogenolysis is such a reaction and has been extensively studied using DFT—often on bare metal surfaces—with the assumption that omitted coadsorbed hydrogen atoms (H*) do not significantly alter the relative activation barriers and with ad hoc assumptions about the site requirements for relevant reactions. Here, we use ethane hydrogenolysis on H*-covered Ir catalysts (using a periodic surface model and a nanoparticle model) as a probe reaction to examine coadsorbate interactions and to demonstrate the rigorous determination of site requirements. The kinetically relevant transition state [*CH−CH*]‡ is larger than the 0−3 coadsorbed H* atoms it replaces, such that the reaction has a positive activation area (a concept analogous to activation volume in homogeneous reactions) and thus repels coadsorbed H* atoms when fewer than four H* vacancies are created. This induced strain cannot be relieved on the periodic surface models, resulting in large effective free energy barriers and predictions that four vacant sites are required ($\gamma = 4$). These barriers and site requirements lead to turnover rates that are 4 orders of magnitude lower than measured rates and incorrect H_2-pressure dependencies. Furthermore, varying the unit cell size of the Ir(111) surface dramatically alters the calculated reaction energetics, indicating that relevant transition states destabilize one another over long distances through the H* adlayer. Curved H*-covered Ir hemispherical particle models (119 atoms), however, stabilize transition states at a lower number of vacant sites ($\gamma = 2$) through lateral relaxation of the adlayer, resulting in correct predictions of H_2-pressure dependencies and quantitative agreement between calculated and measured rates.

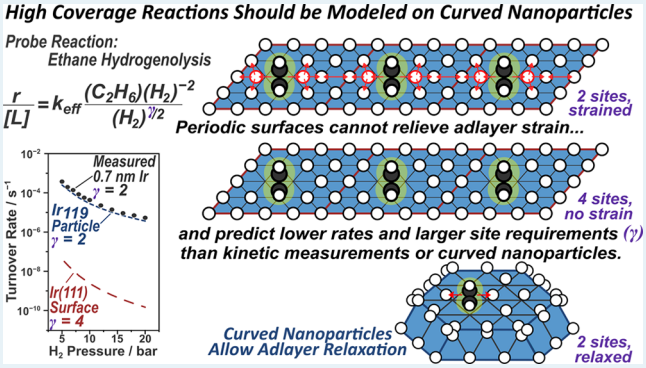

KEYWORDS: *coverage effects, coadsorbate interactions, catalyst model, density functional theory, hydrogenolysis, metal catalysis*

1. INTRODUCTION

Surface-catalyzed reactions on supported metal clusters often occur at near-saturation conditions, where high coverages significantly affect binding energies of adsorbed species and their reactivity.[1−12] Previous studies show that adsorbed intermediates tend to react with coadsorbed species at high coverages instead of reacting with scarce vacant sites. O_2 dissociation across a pair of metal sites, for example, is essentially barrierless on nearly bare Pt surfaces[6,13−15] but occurs with a very high overall activation barrier on CO*-covered Pt surfaces because CO* must desorb prior to O_2 activation. Because vacancies are rare on such surfaces, O_2 dissociates instead via bimolecular reactions with coadsorbed CO*,[16] reducing the need for CO* desorption. High coverages weaken bonds between adsorbed species and surface atoms via a combination of through-space and through-surface interactions, as reported previously for CO* on Ru nanoparticles and Pt(111) surface,[17−20] thus increasing the desorption rate of bound species to create vacant sites required to adsorb reactants or dissociate species.[9,12]

Langmuirian kinetic models do not account for coadsorbate interactions that prevail at high surface coverages and thus provide inaccurate descriptions for reactions in dense adlayers. Previous studies show that rates of surface reactions in dense adlayers can depend on the area of activation,[18] in an analogy with the activation volume often used to describe pressure effects for nonideal homogeneous reactions via

$$\left(\frac{\partial \ln k}{\partial P}\right)_T = \frac{-\Delta V^{\ddagger}}{RT} \quad (1)$$

where k is the reaction rate constant and P is the pressure. The rate constant increases with increasing pressure if the formation of the transition state involves a net contraction in volume

Received: March 20, 2018
Revised: May 23, 2018
Published: May 30, 2018

DOI: 10.1021/acscatal.8b01114
ACS Catal. 2018, 8, 6375−6387

(i.e., $\Delta V^{\ddagger}$ is negative), and k decreases with increasing pressure if $\Delta V^{\ddagger}$ is positive. A decrease in volume often occurs during associative reactions while dissociative reactions involve an increase in volume. This concept can also be applied to surface reactions where surface tension (τ) rather than pressure affects rates in relation to the change in surface area ($\Delta A^{\ddagger}$) instead of the volume[18]

$$\left(\frac{\partial \ln k}{\partial \tau}\right)_T = \frac{-\Delta A^{\ddagger}}{RT} \quad (2)$$

Measured CO hydrogenation rates on Ru clusters at high CO pressures are much higher than those predicted by Langmuirian treatments,[18] reflecting the inadequacy of Langmuirian models to capture the nonidealities present in dense adlayers. H_2-assisted CO* activation on Ru occurs through transition states ([*HCO−H*]‡) that occupy less surface area than the pair of adsorbed CO* which they replace, resulting in a negative activation area for that surface reaction and causing overall activation energies to decrease with increasing CO* coverage because the transition states are less penalized by high CO* coverages than the pair of CO* they replace.

These effects of coadsorbed species have been documented in theoretical treatments on small nanoparticle catalyst models[17−19] whose curvature weakens coadsorbate repulsions through lateral relaxation of the adlayer, enabling high coverages to form. Previous theoretical studies have focused on using flat periodic surfaces[6,21−24] and at coverages well below saturation,[25−28] and these studies cannot accurately capture the effects of high coverages present at practical catalysis conditions because of artifacts associated with their periodic nature. Metal nanoparticles (>200 atoms in size, ∼2 nm in diameter) with curved surfaces saturated by relevant intermediates, in contrast, account for coadsorbate interactions and allow one to accurately analyze the number of vacant sites required for a chemical reaction. Larger metal particles (>5 nm), often used in heterogeneous catalysis despite their intrinsic economic inefficiencies caused by low dispersion, may also be more accurately studied by these nanoparticle models rather than periodic flat surfaces,[29] as multiple studies have indicated that the terraces of large particles restructure under reaction conditions,[21,30−32] leading to more curved surfaces.

The catalytic hydrogenolysis of alkanes on transition-metal surfaces is used to decrease the chain length of *n*-alkanes and convert them into branched acyclic alkanes, which consequently increases the octane number of fuel.[33−38] Hydrogenolysis, however, is also considered an undesired side reaction in reforming and isomerization of petroleum refinery streams.[39−41] This reaction, furthermore, has been extensively studied for a range of cyclic and acyclic branched and nonbranched alkanes on Ir, Ru, Rh, and Pt supported catalysts varying in size.[42−56] Here, we use alkane hydrogenolysis as a probe reaction to demonstrate the rigorous determination of site requirements for a given surface reaction, expose artifacts associated with high coverage single crystal models—providing additional evidence for the utility of high-coverage nanoparticle models—and therefore provide fundamental insights into modeling other reactions that occur on saturated surfaces, such as CO oxidation,[1,2,4,13] NO reduction and oxidation,[6,9−12,57,58] and C−O hydrogenolysis.[7,59−61]

2. ALKANE HYDROGENOLYSIS

Previous studies on alkane hydrogenolysis have combined kinetic measurements (at high H* coverage on supported metal particles) with theoretical studies (at low H* coverage on single-crystal surfaces) and have shown that C−C bond cleavage within *n*-alkanes (C_2−C_{10}),[42−52] branched alkanes (C_4−C_6),[50,53−55] and alkyl cyclohexane[53,56] occurs via unsaturated species formed by sequential quasi-equilibrated dehydrogenation steps;[42−45,49,53,54,56] the removal of H atoms weakens the C−C bonds by replacing C−H bonds with C−metal bonds.[62,63] These removed H atoms desorb from the metal surface to form H_2(g) that increases activation entropies, thus lowering the activation free energies and increasing reaction rates. Chemisorbed hydrogen (H*) must also desorb from saturated surfaces (typical of high-pressure alkane hydrogenolysis)[44,45,49,53,54,56] to accommodate the adsorption and subsequent C−C cleavage of alkane-derived species. The H-content of the reactive intermediate and the number of sites required for the rate-determining transition state can be inferred by measuring the effect of H_2 pressure on C−C hydrogenolysis rate,[42,43,64,65] but each value (H-content, vacancy requirement) cannot be measured independently because current spectroscopic methods lack the ability to detect reactive species that exist in low concentrations during catalysis. As a result, theoretical methods have been used in combination with kinetic measurements to reveal the identity of the reactive intermediate and the nature of active sites.[45,46,49,54,66,67]

Scheme 1 shows a sequence of elementary steps for C−C hydrogenolysis in ethane. The equilibrated cycloalkane−arene

Scheme 1. Proposed Mechanism for Ethane Hydrogenolysis on Metal Catalysts[45],[a]

$$H_2 + 2^* \overset{K_{H_2}}{\leftrightarrows} 2H^* \quad (1.1)$$

$$C_2H_6 + * \overset{K_{C_2H_6}}{\leftrightarrows} C_2H_6^* \quad (1.2)$$

$$C_2H_6^* + (\gamma - 1)^* \overset{K_{CH,y}}{\leftrightarrows} C_2H_{6-y}^{\gamma^*} + 0.5y\,H_2 \quad (1.3)$$

$$C_2H_{6-y}^{\gamma^*} \xrightarrow{k_{CC,y}} CH_a^{c^*} + CH_b^{d^*} \quad (1.4)$$

$$CH_a^{c^*} + xH^* \overset{K_{CH_4}}{\leftrightarrows} CH_4 + (x+c)^* \quad (1.5)$$

[a]The double arrow with an overlaid circle indicates a quasi-equilibrated reaction, * a vacant site on a H*-covered surface, γ* an adsorbate occupying γ vacant site, and K_x and k_x are equilibrium and rate constants for individual steps.

mixtures during alkane hydrogenolysis on Ir, Ru, Rh, and Pt clusters[44,45,49,53,56] indicate that H_2 dissociation (1.1), ethane adsorption (1.2), and ethane dehydrogenation (1.3) steps are all quasi-equilibrated, leaving the C−C bond cleavage (1.4) as the kinetically relevant step. At high H_2/alkane ratios, chemisorbed hydrogen (H*) is the sole most abundant surface intermediate (MASI), and ethane hydrogenolysis rates depend linearly on ethane pressure and inversely on H_2 pressure[45]

$$\frac{r_y}{[L]} = k_{CC,y}\frac{(\prod_{i=1}^{y} K_{CH,i})K_{C2H6}(C_2H_6)}{K_{H2}(H_2)^{\lambda}} \quad (3)$$

where r_y/[L] is the turnover rate normalized by the number of exposed metal atoms, ($\Pi_{i=1}^{y} K_{CH,i}$) is the product of the equilibrium constants for the C−H activation steps, and λ is the number of H_2(g) molecules evolved during the y C−H bond rupture steps and the desorption of γ H* atoms from the surface, such that

$$\lambda = 1/2(y + \gamma) \quad (4)$$

Measured ethane hydrogenolysis rates show that 3 H_2(g) molecules evolve (λ = 3) during the formation of the reactive

DOI: 10.1021/acscatal.8b01114
ACS Catal. 2018, 8, 6375−6387

intermediates that undergo C−C bond cleavage on SiO_2-supported Ir clusters (0.7 and 7 nm in diameter).[44,45] The values of y and γ, however, cannot be determined independently from rate measurements, and therefore, DFT calculations at low coverage using the Ir(111) surface examined C−H and C−C activations in all C_2H_{6-y} intermediates and showed that C−C bond cleavage occurs via the *CHCH* intermediate (y = 4), which has the lowest free energy barrier.[45] Subsequent experimental and DFT studies confirmed that C−C bond cleavage in larger n-alkanes also occurs via RC*−C*R′‡ transition states, which lost 4 H atoms (y = 4).[44,49,53,54] These calculations accounted for the energy to form H* vacancies by calculating H* desorption from H*-covered surfaces, but were otherwise carried out using a H*-bare Ir(111) surface with the assumption that coadsorbed H* atoms would not significantly alter the relative free energy barriers for C−C cleavage in C_2H_{6-y}* surface intermediates, an assumption confirmed by the current study. The measured overall H_2-dependence (λ = 3) and DFT predictions that C−C bonds cleave in *CHCH* species (y = 4) suggest (by eq 4) that 2 H* must desorb from H*-saturated Ir surfaces to accommodate ethane and the *CHCH* activation transition state (γ = 2). Neither experiment nor theory have yet to unequivocally demonstrate that exactly two H* atoms must desorb from the surface to bind the vicinal C atoms in the C−C bond being cleaved. The number of vacant sites required for a surface reaction is often assumed based on the number of bonds the reactive intermediate forms with the surface (4, in this case) or the number of C atoms interacting with the surface (2, in this case). Rigorously, however, the number of sites required is described as the number of MASI-desorption events prior to reaction to accommodate the transition state as shown in the rate equation (eq 3). DFT can only predict such site requirements, therefore, by varying the number of preceding desorption events (by varying the number of H*-vacancies) and comparing the free energy barriers that accurately account for these desorption events.

This work confirms prior studies that show that C−C bonds cleave in *CHCH* species, however, we show that these species and the transition states which mediate C−C cleavage communicate through the H* adlayer across large distances on periodic crystal models, leading to significant artifacts. High-coverage single crystal models, furthermore, predict that four H* atoms must desorb from the surface to facilitate ethane hydrogenolysis (i.e., that ethane hydrogenolysis requires four sites on the catalytic surface), leading to DFT-predicted λ values of 4, inconsistent with measured values on small and large Ir particles (λ = 3).[44,45] Hemispherical models, in contrast, allow adlayers to laterally relax, removing any artifacts associated with periodic boundary conditions, and correctly predict that ethane hydrogenolysis requires the desorption of two H* (γ = 2), leading to predicted rates and λ values that are in good agreement with measured values.

3. COMPUTATIONAL METHODS

Periodic, planewave density functional theory (DFT) calculations were performed using the Vienna ab initio simulation package (VASP).[68,69] Planewaves were constructed using projector augmented-wave (PAW) potentials with an energy cutoff of 396 eV.[70−72] The revised Perdew−Burke−Ernzerhof (RPBE) form of the generalized gradient approximation (GGA) was used to describe exchange and correlation energies.[73,74] Wave functions were converged until electronic energies varied less than 10^{-6} eV. Forces on all atoms were determined using a fast Fourier transform (FFT) grid with a cutoff equal to twice the planewave cutoff and structures were geometrically optimized until the forces on all atoms were less than 0.05 eV Å^{-1}. Gas-phase calculations of C_2H_6 and H_2 were modeled within an 18 × 18 × 18 Å unit cell of empty space, and the Brillouin zone for such calculations was sampled at the Γ-point.

Ir (111) surfaces were modeled as 4 × 4 periodic lattices with four layers orthogonal to the surface and 10 Å of vacuum separating slabs (Figure 1a,c); the bottom two layers were fixed in their bulk positions and the top two layers were relaxed. A 3 × 3 × 1 Monkhorst−Pack sampling of the first Brillouin zone (k-point mesh)[75] was used during geometric convergence, and after geometric convergence, a single-point calculation with a 6 × 6 × 1 k-point mesh was performed to determine the electronic energy. Additional calculations (discussed in section 4.2) were performed using 3 × 3 and 6 × 6 unit cells. H* preferentially binds in the atop site on low-index Ir surfaces[76,77] and thus the (111) terraces were modeled as either bare or occupied by atop-bound H* atoms up to a coverage of 1 ML. This saturation coverage (1 ML) is consistent with prior experimental studies of single crystal surfaces[78,79] and unsupported metal particles,[80] as well as previous DFT calculations.[81]

A symmetric cuboctahedral Ir_{201} particle (1.59 nm in diameter) consisting of eight hexagonal (111) terraces and six square (100) terraces connected by under-coordinated edge and corner atoms was optimized at a H* coverage of 1.69 ML by relaxing all atoms to forces < 0.05 eV Å^{-1}. This saturation coverage (1.69 ML) is caused by edge atoms that bind 2 atop H* atoms and corner atoms that bind 3 atop H* atoms, as previously reported using DFT.[81] The cuboctahedral particle was then simplified by removing the bottom three layers in the (111) direction to form Ir_{119} hemispherical particle (Figures 1b and 1d). The bottom two layers of the hemispherical particle and the H* atoms bound to them were kept fixed at their positions in the full particle to prevent any structural changes associated with the formation of the hemispherical particle. The Brillouin zone was sampled only at the Γ-point for all particle calculations. This simplified Ir_{119} hemispherical model allows more accurate analysis of high-coverage catalytic reactions without prohibitive computational cost; optimization calculations using the 4 × 4 Ir(111) surface are only 50% faster compared to the hemispherical Ir_{119} model.

Transition-state structures for each elementary reaction were obtained by combining the nudged elastic band (NEB)[82,83] and dimer[84] methods. The NEB method was carried out using 16 images, and wave functions were converged to within 10^{-4} eV. The maximum force on each atom was converged to < 0.5 eV Å^{-1}. These convergence criteria provided an estimate of the reaction path and starting points for reaction mode and structure for each transition state. The dimer algorithm was then used with wave functions converged to within 10^{-6} eV, and the maximum force on each atom was converged to < 0.05 eV Å^{-1}, consistent with all minima optimizations.

Frequency calculations were performed on gas phase molecules and all optimized adsorbed species to determine zero-point vibrational energies (ZPVE), and vibrational, translational and rotational enthalpy, and free energy. These terms were then used, together with electronic energies (E_0, provided by VASP), to estimate enthalpies

$$H = E_0 + \mathrm{ZPVE} + H_{\mathrm{vib}} + H_{\mathrm{trans}} + H_{\mathrm{rot}} \quad (5)$$

and free energies

$$G = G_0 + \mathrm{ZPVE} + G_{\mathrm{vib}} + G_{\mathrm{trans}} + G_{\mathrm{rot}} \quad (6)$$

DOI: 10.1021/acscatal.8b01114
ACS Catal. 2018, 8, 6375−6387

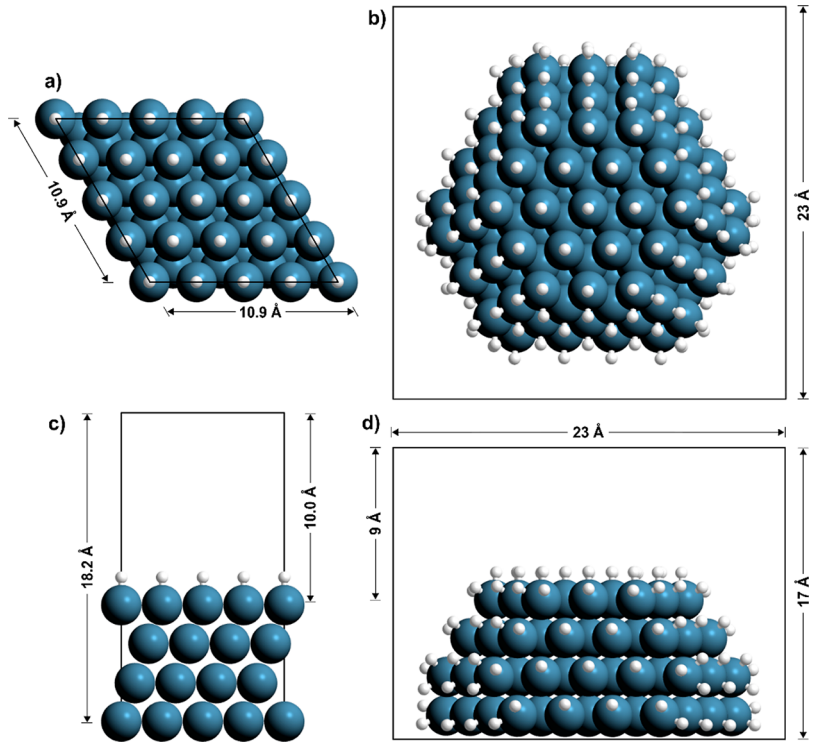

Figure 1. Top and side views of the H*-covered 4 × 4 Ir(111) surface (a and c) and the Ir_{119} hemispherical particle (b and d). The bottom two layers of the Ir(111) surface were fixed at their bulk positions during geometric convergence. The bottom two layers of the Ir_{119} hemispherical particle and all H* bound to them were fixed in their Ir_{201} positions during geometric convergence. All atoms except adsorbed species and H* on the top (111) terrace were constrained during frequency calculations.

for all reactants, products, and transition states at 593 K (a temperature representative of recent ethane hydrogenolysis experiments[45]).

C−C bond cleavage occurs in partially dehydrogenated intermediates ($C_2H_{6-y}^{\gamma*}$; $0 \le y \le 6$) as shown in Scheme 1 at rates described by

$$\frac{r_y}{[L]} = k_{CC,y}[C_2H_{6-y}^{\gamma*}] \tag{7}$$

where $k_{CC,y}$ is the C−C cleavage rate constant in the intermediate that lost y hydrogen atoms via the preceding C−H activation steps and γ is the number H* atoms desorbed from the surface to accommodate the reactive intermediate. The formalism of transition state theory and the quasi-equilibrated nature of steps 1.1−1.3 in Scheme 1 dictate that gas phase ethane and γ H* atoms are quasi-equilibrated with the C−C cleavage transition state ($[C_2H_{6-y}^{\gamma*}]^{\ddagger}$) and the product H_2

$$C_2H_6 + \gamma\, H^* \rightleftharpoons [C_2H_{6-y}^{\gamma*}]^{\ddagger} + \lambda\, H_2 \tag{8}$$

where $K^{\ddagger}$ is the equilibrium constant for the formation of the transition state from gas phase ethane and a H*-covered surface. Therefore, rates for C−C bond cleavage are related to the activation free energy ($\Delta G^{\ddagger}$) by

$$\frac{r_y}{[L]} = \frac{k_B T}{h} \exp\left(\frac{-\Delta G^{\ddagger}}{RT}\right)\frac{(C_2H_6)}{(H_2)^{\lambda}} \tag{9}$$

Here, $\Delta G^{\ddagger}$ is defined as the free energy of forming the partially dehydrogenated transition state ($[C_2H_{6-y}^{\gamma*}]^{\ddagger}$) at γ vacant sites and a stoichiometric amount of gas phase H_2 from gas phase ethane and a fully covered surface (nH*)

$$\Delta G^{\ddagger} = G[C_2H_{6-y}^{\gamma*}]^{\ddagger} + \lambda G[H_2] - G[n\mathrm{H}^*] - G[C_2H_6] \tag{10}$$

$\Delta G^{\ddagger}$ can be separated into two components to simplify analysis

$$\Delta G^{\ddagger} = \Delta G^{\gamma*} + \Delta G_k \tag{11}$$

where $\Delta G^{\gamma*}$ is the free energy required to form γ vacant sites

$$\Delta G^{\gamma*} = G[(n-\gamma)\mathrm{H}^*] + 0.5\gamma G[H_2] - G[n\mathrm{H}^*] \tag{12}$$

and ΔG_k is the free energy to form the transition state once the vacancies have been formed

$$\Delta G_k = G[TS^{\gamma*}] + 0.5yG[H_2] - G[(n-\gamma)\mathrm{H}^*] - G[C_2H_6] \tag{13}$$

Analogous equations for $\Delta H^{\ddagger}$ and $\Delta S^{\ddagger}$ exist through their relation to $\Delta G^{\ddagger}$

$$\Delta G^{\ddagger} = \Delta H^{\ddagger} - T\Delta S^{\ddagger} \tag{14}$$

The equations used to determine ZPVE, H_{vib}, and G_{vib} from vibrational frequencies for all species and H_{trans}, H_{rot}, G_{trans}, and G_{rot} from statistical mechanics for gas phase molecules are reported in the Supporting Information (SI, section S1).

4. RESULTS AND DISCUSSION

4.1. H* Desorption Energies at High Coverages.

Chemisorbed H* covers surfaces during high-pressure alkane hydrogenolysis experiments,[44,45,49,53,54,56] and H* must therefore desorb from such surfaces to allow alkanes to react. Here, we examine DFT-predicted free energies to create γ vacancies ($\Delta G^{\gamma*}$, eq 12) on H*-covered Ir(111) and Ir_{119} surfaces, such that

$$\gamma\, H^* \rightleftharpoons \tfrac{1}{2}\gamma\, H_2 + \gamma\, * \tag{15}$$

DOI: 10.1021/acscatal.8b01114
ACS Catal. 2018, 8, 6375−6387

Multiple configurations for each number of vacancies were examined on the Ir_{119} hemispherical particle to predict the most favorable state. For example, there are five distinct binding sites for a single H* atom on the (111) facet that have different coordination numbers: one corner (CN = 6), two edge (CN = 7), and two distinct terrace (CN = 9) sites (Figure 1b). Calculated ΔG^{γ}* values (eq 12) are negative, indicating favorable desorption, and decrease with increasing H* atoms desorbed on both catalyst models (Figure 2a); ΔG^{γ}* decreases from −18 to −243 kJ mol^{-1} at γ = 1−16 on the Ir(111) surface and decreases from −18 to −231 kJ mol^{-1} at γ = 1−19 on the Ir_{119} particle (Figure 2a). These desorption energies are not normalized, and therefore, their decrease with increasing γ reflects that removing two H* decreases free energy by approximately twice that of removing a single H*. These large, negative desorption free energies indicate that DFT predicts a bare Ir surface at 593 K and 1 bar H_2. These ΔG^{γ}* values remain negative at ambient temperatures (300 K) typical of H_2 chemisorption experiments, once again indicating that DFT predicts surfaces should be bare, in stark contrast to the experimental observations during H_2 chemisorption studies which show that H_2 covers Ir and other metal surfaces at near-ambient conditions.[85−88] At C−C hydrogenolysis conditions (593 K), the H_2-pressure dependence of ethane hydrogenolysis ($\lambda \sim 3$, eqs 3 and 4) is constant across the entire range of H_2 pressures (4−20 bar H_2),[44,45] indicating that H* coverage does not significantly change over this factor-of-five increase in H_2 pressure, which is consistent with a surface that is either essentially bare or essentially saturated. While a bare surface would be consistent with DFT predictions showing large negative desorption free energies, the measured value of λ (3) would (under a bare surface assumption) indicate that the C−C bonds of ethane cleave in fully dehydrogenated *CC* intermediates (y = 6, γ = 0, λ = 3, eq 4). This suggestion, however, is inconsistent with prior DFT studies that showed that the overall activation free energy to form and activate the *CC* intermediate is 176 kJ mol^{-1} larger than the free energy to form and activate the *CHCH* intermediate,[45] indicating that C−C bonds do not activate in *CC* and essentially ruling out a bare surface interpretation of the kinetic results. H_2 chemisorption and C−C hydrogenolysis experiments both contradict DFT-predictions of bare Ir surfaces.

This discrepancy reflects inaccurate DFT predictions of H* adsorption enthalpy and/or entropy. The RPBE functional used here neglects attractive dispersive interactions among coadsorbed H* atoms and therefore underestimates adsorption enthalpies by up to 10−20 kJ mol^{-1}.[89] Furthermore, previous studies show that the harmonic oscillator approximation often used to estimate the entropies of adsorbed H* significantly underestimates their entropy.[90] High-temperature H_2 chemisorption measurements on supported Pt nanoparticles show that the entropy of adsorbed H* (S[H*]) is near 60 J mol^{-1} K^{-1}, a value that far exceeds the value estimated from vibrational frequency analysis of adsorbed hydrogen provided by DFT (~15 J mol^{-1} K^{-1} at 593 K). Therefore, to correct for this underestimation, entropy of adsorbed H* is adjusted by a factor-of-four in this work leading to an S[H*] value of 60 J mol^{-1} K^{-1}, consistent with the measured value on supported Pt nanoparticles. Adjusted vacancy formation free energies (ΔG^{γ}*) are positive and increase with additional vacancies on both the Ir(111) surface (7−252 kJ mol^{-1}) and on Ir_{119} particle (8−193 kJ mol^{-1}) (Figure 2b), and these positive values are consistent with an Ir surface saturated in H* at high-pressure hydrogenolysis conditions.

4.2. Effects of Coadsorbed H* Atoms and Transition-State Density on *CH−CH* Bond Activation. A previous DFT study of ethane hydrogenolysis on a bare Ir(111) surface[45] examined all C−H and C−C bonds activations for all C_2H_{6-y}* intermediates (where $0 \le y \le 6$) and showed, based on calculated free energy barriers ($\Delta G^{\ddagger}$, eq 10), that C−C bond cleavage occurs via

$$CH_3CH_3 + 2H^* \rightleftharpoons {}^*CHCH^* + 3H_2 \quad (16)$$

$$^*CHCH^* \rightarrow 2CH^* \quad (17)$$

where eq 16 represents the quasi-equilibrated formation of *CHCH* intermediate and stoichiometric amount of H_2 in the gas phase as shown in steps 1.1−1.3 in Scheme 1. C−C bond activation in *CHCH* intermediate (eq 17) is the rate-determining

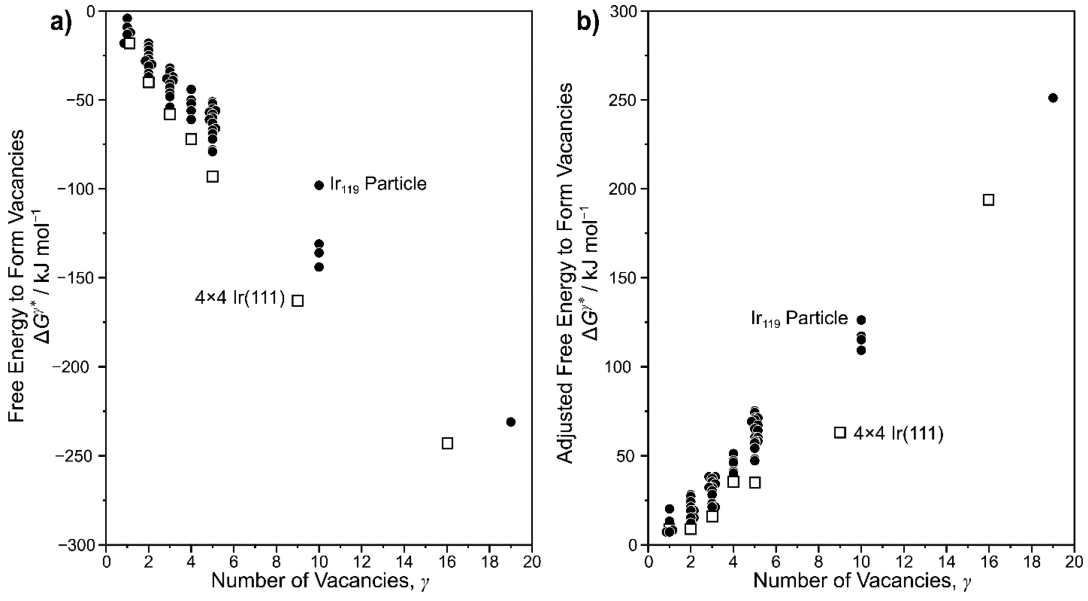

Figure 2. Free energy ΔG^{γ}* to form vacancies (eq 12) on H*-covered Ir(111) surface (□) and Ir_{119} particle (●) before (a) and after (b) adjusting the DFT-predicted entropy of H* (593 K, 1 bar H_2).

DOI: 10.1021/acscatal.8b01114
ACS Catal. 2018, 8, 6375−6387

step (step 1.4 in Scheme 1), and it occurs after four successive C−H bond activations ($y = 4$). It was assumed that cleavage via this intermediate requires two vacant sites ($\gamma = 2$) based on the interaction of two C atoms with the surface in *CHCH* and the product (2 CH*), giving a λ value of 3 (eq 4). This DFT-predicted λ value is consistent with the measured λ (0.2 bar C_2H_6, 4−20 bar H_2, 593 K) on 0.7 nm Ir clusters (3.0 ± 0.2)[44] and on 7 nm Ir clusters (3.3 ± 0.2).[45] The noninteger value of the measured λ value on 7 nm Ir clusters may indicate that edge and corner metal atoms found in nonuniform Ir clusters can bind more than one H atom, as previously shown using DFT,[81] and would give a different γ value than metal atoms located at terraces which can bind a single H atom. Another possibility is that *CH−CH* bond activation actually requires the removal of more than two H* atoms from the surface but the Ir surface is not fully saturated with H* during ethane hydrogenolysis, which is unlikely because hydrogen is known to saturate Ir and Pt surfaces even at H_2 pressures significantly lower (1 bar)[85−88] than those used here (4−20 bar H_2). While *CHCH* species interact with the surface through two C atoms—leading to the assumption that $\gamma = 2$—they also interact with four surface metal atoms, suggesting that $\gamma = 4$ (as in Figure 3e), which would lead to λ values of 4, more than measured values on either Ir particles (~3).[44,45] No direct evidence was provided to support the assumption that *CHCH* occupies two sites on the catalyst surface because the previous study was done on bare surfaces.[45] These discrepancies can only be resolved by rigorous DFT analysis using H*-covered surfaces to examine the effects of coadsorbed H* atoms on the stability of the $[*CH{-}CH*]^{\ddagger}$ transition state and to determine the number of vacant sites required.

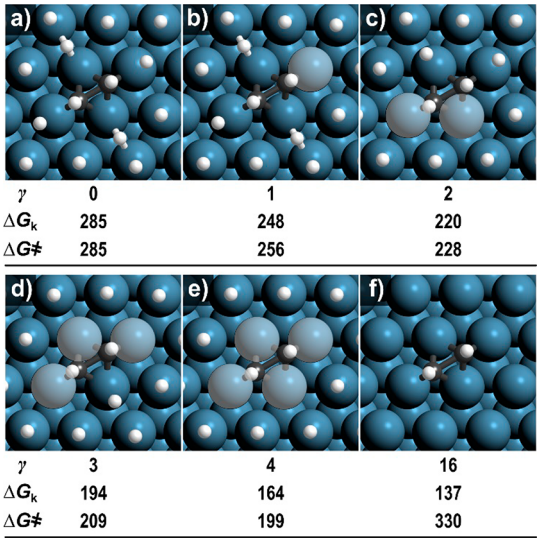

Figure 3. Rate determining *CH−CH* bond cleavage transition state on the 4 × 4 Ir(111) surface at different number of vacancies (γ = 0−4 and 16, for a−f). ΔG_k (eq 13) and $\Delta G^{\ddagger}$ (eq 10) values are shown beneath each image in kJ mol^{-1} (593 K, 1 bar H_2). Shadings represent vacant sites.

Figure 4 shows the free energy to form the $[*CH{-}CH*]^{\ddagger}$ transition state from ethane once the vacancies have been formed (ΔG_k, eq 13) as a function of γ. These energies do not include the free energy to desorb H* from the surface (ΔG^{γ}*, eq 12) and only show the stability of the transition state at a given number of vacant sites, elucidating coadsorbate interactions between the transition state and the surrounding H* adlayer. Vacancies can be formed in multiple positions around the $[*CH{-}CH*]^{\ddagger}$ transition state, and all reasonable configurations have been modeled in this work, prioritizing configurations with vacancies near the transition state, where they are most likely to form to reduce coadsorbate repulsions. ΔG_k decreases rapidly on the 4 × 4 Ir(111) surface with a slope of −30 kJ mol^{-1} γ^{-1} (Table 1) with increasing the number of desorbed H* from the surface (γ) for $0 \le \gamma \le 4$; ΔG_k changes from 285 kJ mol^{-1} at $\gamma = 0$ to 164 kJ mol^{-1} at $\gamma = 4$ (Figure 4). The dramatic decrease in ΔG_k indicates that coadsorbed H* atoms significantly destabilize the $[*CH{-}CH*]^{\ddagger}$ transition state when fewer than four H* atoms desorb from the surface, as suggested by $[*CH{-}CH*]^{\ddagger}$ transition states binding to four metal atoms (Figure 3) and vicinal H* atoms appear to be repelled by the transition state at those coverages (Figure 3a−d). This destabilization effect becomes much weaker at $\gamma \ge 4$ where ΔG_k decreases from 164 kJ mol^{-1} at $\gamma = 4$ to 137 kJ mol^{-1} at $\gamma = 16$ (Figure 4) with a slope of −3 kJ mol^{-1} γ^{-1}. The Ir_{119} hemispherical particle model exposes under-coordinated edge and corner atoms in addition to atoms within the (111) terraces. Here, we consider such sites separately, as the number of terrace

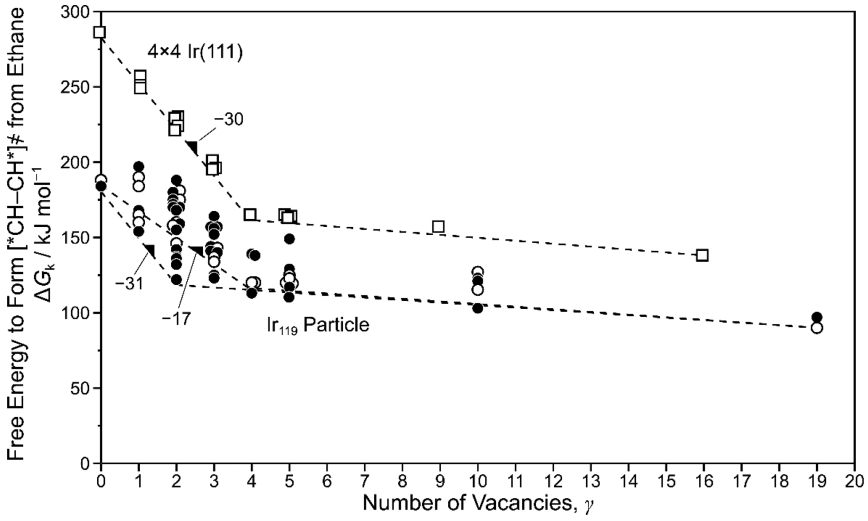

Figure 4. Free energy ΔG_k (eq 13) to form the transition state $[*CH{-}CH*]^{\ddagger}$ and $2H_2$ from ethane once the vacancies have been formed (593 K, 1 bar H_2) on Ir(111) surface (□) and Ir_{119} particle (○). Filled data points (●) indicate CH*−CH* bond activation near corners and edges on Ir_{119}. Dashed lines are drawn to guide the eye and their slopes are indicated in kJ mol^{-1} γ^{-1}.

DOI: 10.1021/acscatal.8b01114
ACS Catal. 2018, 8, 6375−6387

Table 1. Change of Enthalpy, Entropy, and Free Energy To Form the [*CH−CH*]‡ Transition State with the Change of the Number of Vacancies γ (593 K, 1 bar H_2)

	γ = 0−4			$\gamma \geq 4$		
model	$\Delta\Delta H_k/\Delta\gamma$ (kJ mol^{-1} vac^{-1})	$\Delta\Delta S_k/\Delta\gamma$ (J mol^{-1} K^{-1} vac^{-1})	$\Delta\Delta G_k/\Delta\gamma$ (kJ mol^{-1} vac^{-1})	$\Delta\Delta H_k/\Delta\gamma$ (kJ mol^{-1} vac^{-1})	$\Delta\Delta S_k/\Delta\gamma$ (J mol^{-1} K^{-1} vac^{-1})	$\Delta\Delta G_k/\Delta\gamma$ (kJ mol^{-1} vac^{-1})
Ir 3 × 3	−36	−3	−38	−3	6	−7
Ir 4 × 4	−29	−3	−30	−2	1	−3
Ir 6 × 6	−26	−3	−24	−1	0	−1
Ir_{119} (t)[a]	−17	−0	−17	−2	0	−2

[a]Reactions involving (111) terrace atoms only.

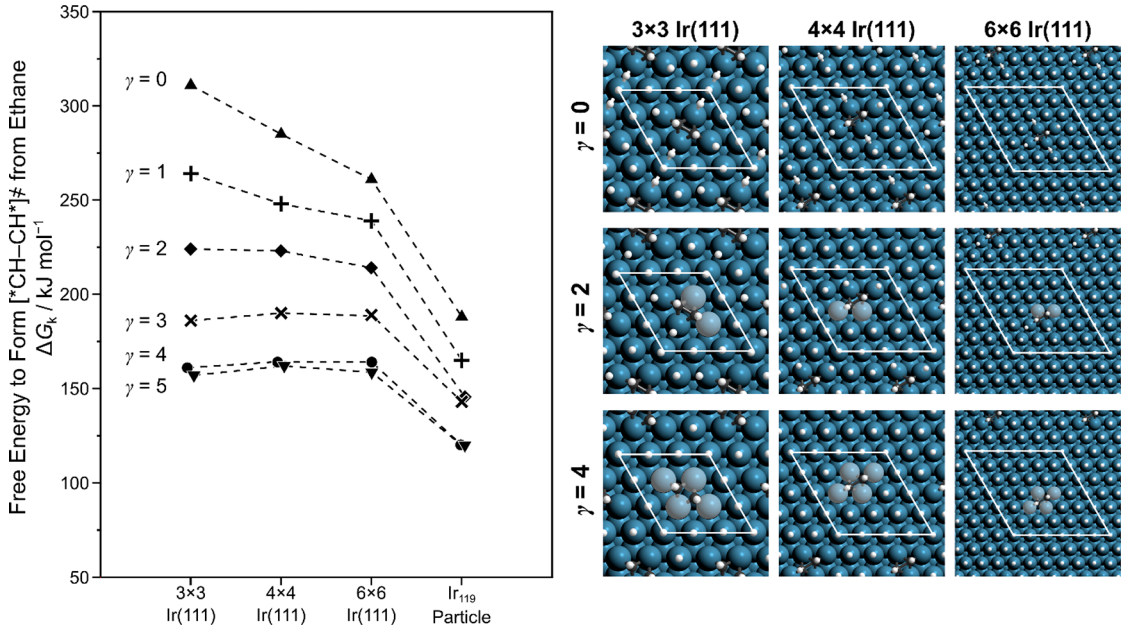

Figure 5. Free energy ΔG_k (eq 13) to form the transition state [*CH−CH*]‡ and $2H_2$ from ethane at γ = 0 (▲), 1 (+), 2 (◆), 3 (×), 4 (●), and 5 (▼) on Ir(111) surfaces of different unit cell sizes and Ir_{119} particle (593 K, 1 bar H_2). Dashed lines are drawn to guide the eye. Shadings represent vacant sites. Transition state structures at other γ values are shown in the Supporting Information (SI, Figures S1−S3).

sites increases dramatically with increasing particle size and terrace sites cover > 87% of the surfaces of 7 nm Ir particles. Furthermore, the terrace-sites are similar to those found in the Ir(111) surface model and are therefore excellent points of comparison. Considering only transition states interacting entirely with the (111) terrace sites, ΔG_k on Ir_{119} exhibits similar trends but with much lower ΔG_k values; ΔG_k decreases rapidly from 188 kJ mol^{-1} at γ = 0 (Figure 4) to 120 kJ mol^{-1} at γ = 4 (a slope of −17 kJ mol^{-1} γ^{-1}, Table 1, less than the slope on the 4 × 4 Ir(111) model, −30 kJ mol^{-1} γ^{-1}), and then it decreases weakly to 90 kJ mol^{-1} at γ = 19 (a slope of −2 kJ mol^{-1} γ^{-1}). The weak destabilizations for $\gamma \geq 4$ on both models are consistent with weak through-surface interactions between H* and ethane-derived species at low H* coverages. The strong destabilizations present at $\gamma \leq 4$ on both models indicate significant through-space repulsions that begin at such coverages, and the weaker degree of destabilization on Ir_{119} (slope of −17 kJ mol^{-1} γ^{-1}) compared to a 4 × 4 Ir(111) surface (slope of −30 kJ mol^{-1} γ^{-1}) is likely related to the ability of the H* adlayer to relax on the curved and nonperiodic Ir_{119} cluster model, whereas the H* adlayer is unable to relax on the periodic Ir(111) surface. The impacts of this periodic strain may be affected by the size of the Ir(111) surface model because the size of the model alters the density of transition states.

The dramatic change in the effects of vacancies at γ = 4 (Figure 4) demonstrates a shift from weak through-surface interactions (at γ values from 4 to 16) to strong through-space interactions ($\gamma \leq 4$). The lower ΔG_k values on the Ir_{119} particle—where there is only one transition state per particle—compared to the periodic Ir(111) surface at a given γ indicate that the transition states communicate through coadsorbate interactions with H* at high coverages despite their large through-space distances. For γ values < 4, the H* atoms near the transition state move away from the transition state and attempt to compress the surrounding H* adlayer (Figure 3a−d). The periodic nature of these surface calculations results in the H* adlayer being compressed from all sides, with no ability to relax the induced strain, resulting in large repulsions and large ΔG_k values as shown previously for oxygen adsorption on Pt(111) surface.[12,21] To further examine the effects of the periodic boundary conditions, we examined *CH−CH* bond cleavage on two additional unit cell sizes for the Ir(111) surface (3 × 3 and 6 × 6) as shown in Figure 5. Both of these unit cell sizes exceed 2 × 2 models often used in DFT literature[91−94] and are sufficiently large to eliminate any direct through-space interactions of the [*CH−CH*‡] bond cleavage transition state. For the fully H*-covered surface (γ = 0), ΔG_k decreases rapidly from 311 kJ mol^{-1} on the 3 × 3 unit cell to 261 kJ mol^{-1} on 6 × 6 unit cell, indicating that decreasing the density of transition states (from 1 per 9 Ir atoms to 1 per 36 Ir atoms) decreases the magnitude of the periodic artifacts associated with the inability

DOI: 10.1021/acscatal.8b01114
ACS Catal. 2018, 8, 6375−6387

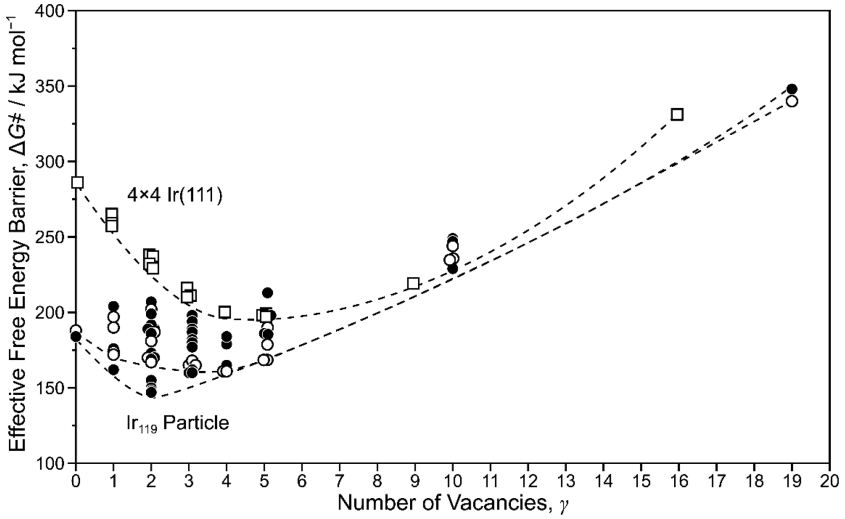

Figure 6. Effective free energy $\Delta G^{\ddagger}$ barriers (eq 10) for C−C bond cleavage in the CH*CH* intermediate (593 K, 1 bar H_2) on Ir(111) surface (□) and Ir_{119} particle (○). Filled data points (●) indicate CH*−CH* bond activation near corners and edges on Ir_{119}. Dashed lines are drawn to guide the eye.

of the H* adlayer to relax under repulsion. The repulsive interaction between the transition state and its surrounding hydrogen atoms is being transferred through the H* adlayer, forming a surface pressure exerted on all periodic transition states (Figure 5), which starts to dissipate with decreasing transition state density; ΔG_k decreases between $\gamma = 0$ and 4 with a slope of −38 kJ mol^{-1} γ^{-1} on the 3 × 3 unit cell compared to −24 kJ mol^{-1} γ^{-1} on the 6 × 6 unit cell (Table 1). This effect becomes weaker with additional vacancies; there is only a 10 kJ mol^{-1} difference between the 3 × 3 and 6 × 6 unit cells at $\gamma = 2$ and almost no effect at $\gamma \geq 4$ (Figure 5). ΔG_k values for the Ir_{119} particle are much smaller than those for the Ir(111), indicating that curved surfaces weaken coadsorbate repulsions through lateral relaxation of the adlayer as reported previously for CO* on Ru and Pt nanoparticles.[17−19] Transition state structures on the Ir(111) surfaces at other γ values are shown in the Supporting Information (SI, Figures S1−S3).

Measured CO hydrogenation rates on Ru clusters at high CO pressures are much higher than those predicted by Langmuirian treatments as a result of the negative activation area ($\Delta A^{\ddagger}$, eq 2) caused by the replacement of a pair of CO* with a transition state ($[*HCO-H*]^{\ddagger}$) that occupies less surface area.[18] Here, the van der Waals radii of carbon and hydrogen atoms are 0.17 and 0.12 nm, respectively,[95] leading to transition-state [*CH−CH*]‡ areas (0.15 nm^2) that are larger than the surface area of 0−3 chemisorbed H* atoms (0, 0.045, 0.091, and 0.14 nm^2, respectively), leading to a positive activation area (for $\gamma < 4$) and resulting in lateral compression of the adlayer that cannot be relieved in flat periodic surfaces. Although empirically measured van der Waals radii of carbon and hydrogen atoms vary in the literature (C = 0.168−0.177 nm; H = 0.11−0.12 nm),[95−98] any choice of empirical radii will produce similar trends. Curved surfaces allow H* adlayers to laterally relax under strain, as observed for reactions modeled on the Ir_{119} particle model. The H* adlayer relaxation on curved surfaces effectively reduces the penalty associated with a positive activation area at γ values <3, as shown by decreasing ΔG_k values by a slope of −17 kJ mol^{-1} γ^{-1} on the Ir_{119} model (terrace sites, Figure 4) compared to a slope of −30 kJ mol^{-1} γ^{-1} on the Ir(111) model. These findings reflect the inadequacy of flat surfaces to capture the lateral relaxation that the adlayer undergoes on the curved surfaces of small particles and on the restructured surfaces of large particles. The surface area occupied by four H* atoms (0.18 nm^2), however, is larger than that of the $[*CH-CH*]^{\ddagger}$ transition state (0.15 nm^2), resulting in a negative activation area for $\gamma \geq 4$. The small size of H* (0.045 nm^2) compared to the size of an Ir atom in the Ir(111) surface (0.064 nm^2) indicates that H* adlayers on surfaces without transition states have weak through-space repulsion and thus weak strain. When strain is present in the adlayer (such as for CO* on Ru), negative activation areas decrease activation free energies because the reaction creates more space on the surface and allows the strained adlayer to laterally relax. Here, the absence of strain in the H* adlayer at $\gamma \geq 4$ results in weak coadsorbate interactions for γ values ≥ 4 (Figure 4) on both the Ir(111) and Ir_{119} models. Next, we examine the effective free energy barriers ($\Delta G^{\ddagger}$; eq 10), i.e., the energy to desorb γ H* from the surface and form the $[*CH-CH*]^{\ddagger}$ transition state (eq 11), to rigorously determine the number of vacancies required for these reactions to occur (γ) and how DFT estimates of γ depend on the model employed.

4.3. Effective Free Energy Barrier for *CH−CH* Bond Activation and the Number of Vacancies Required. Figure 6 shows effective free energy barriers $\Delta G^{\ddagger}$ for ethane hydrogenolysis via *CHCH* activation transition states as a function of the number of vacancies γ on the Ir(111) surface and Ir_{119} particle. These $\Delta G^{\ddagger}$ values include the free energy to form vacancies (ΔG^{γ^*}) and the free energy to form the transition state (ΔG_k), and therefore correspond to turnover rates. $\Delta G^{\ddagger}$ decreases rapidly on the Ir(111) surface from 285 kJ mol^{-1} at $\gamma = 0$ to 199 kJ mol^{-1} at $\gamma = 4$, reflecting the reduction in through-space repulsions and the dramatic decrease in ΔG_k. The free energy penalty to desorb additional H* atoms from the surface starts to prevail at $\gamma > 5$ despite the entropy gain associated with H_2 evolution, rendering the effective free energy barrier the lowest at $\gamma = 5$ (196 kJ mol^{-1}). Although $\Delta G^{\ddagger}$ at $\gamma = 5$ (196 kJ mol^{-1}) is slightly lower than at $\gamma = 4$ (199 kJ mol^{-1}), the turnover rate also depends inversely on H_2 pressure as shown in eq 9. Increasing the number of vacant sites (γ) increases λ (eq 4) and consequently lowers the DFT-predicted turnover rate. The sum of turnover rates for all examined configurations at each γ value is shown in Figure 7 at different

DOI: 10.1021/acscatal.8b01114
ACS Catal. 2018, 8, 6375−6387

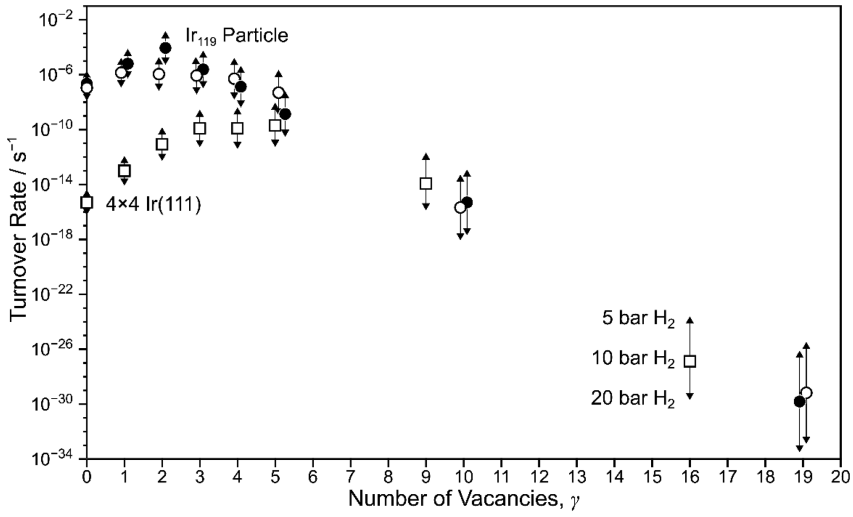

Figure 7. DFT-predicted turnover rates (eq 9) for C−C bond cleavage in the CH*CH* intermediate (593 K, 10 bar H_2, 0.2 bar C_2H_6) on Ir(111) surface (□) and Ir_{119} particle (○). Filled data points (●) indicate CH*−CH* bond activation near corners and edges on Ir_{119}. Up/down arrows represent 5 and 20 bar H_2, respectively.

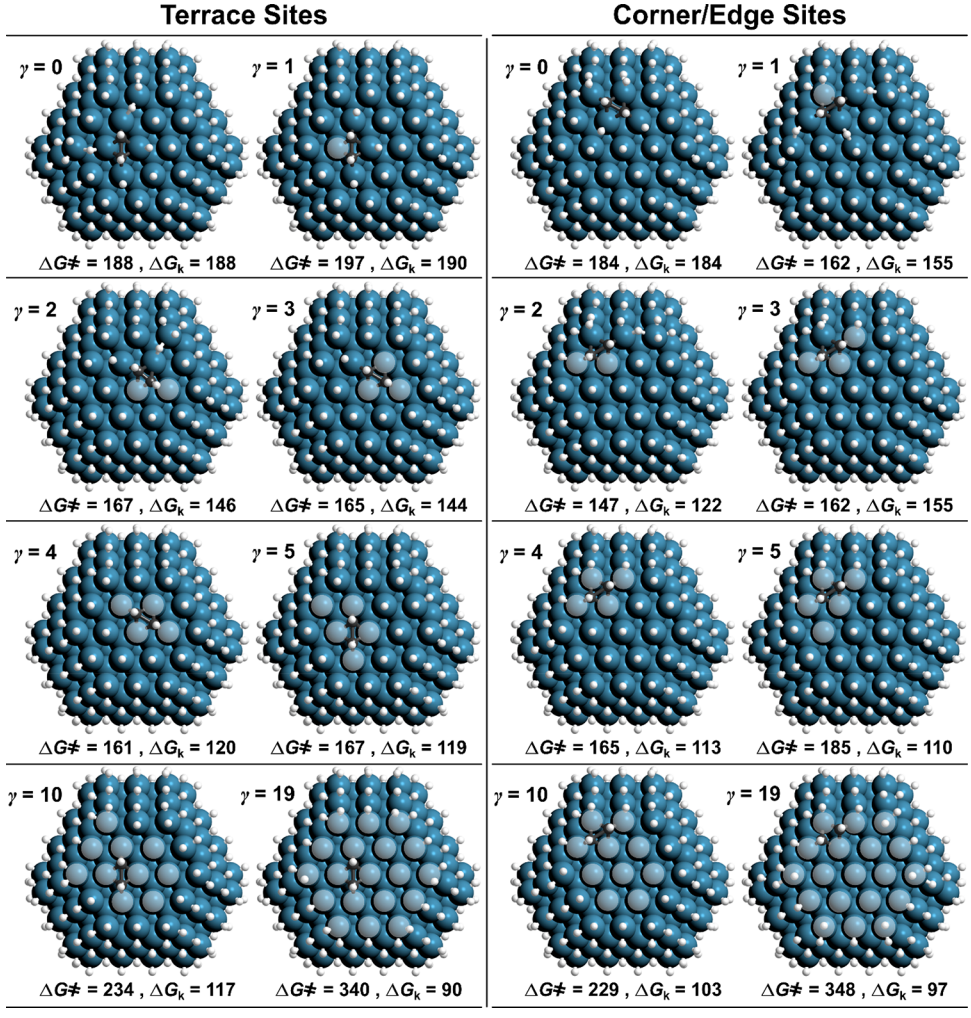

Figure 8. $[*CH-CH*]^{‡}$ transition-state structures on terrace and corner/edge sites at different number of vacancies (γ) on the Ir_{119} particle. $\Delta G^{‡}$ (eq 10) and ΔG_k (eq 13) values are shown beneath each image in kJ mol^{-1} (593 K, 1 bar H_2). Shadings represent vacant sites. Images of other examined configurations are shown in the Supporting Information (SI, Figures S4 and S5).

H_2 pressures (5, 10, and 20 bar). The H_2 pressure dependence renders the turnover rates the highest at γ = 3–5 (~7 × 10^{-10} s^{-1}, 10 bar H_2) (Figure 7), which gives an average λ value of 4 for hydrogenolysis on the 4 × 4 Ir (111) surface model. The $\Delta G^{‡}$

DOI: 10.1021/acscatal.8b01114
ACS Catal. 2018, 8, 6375−6387

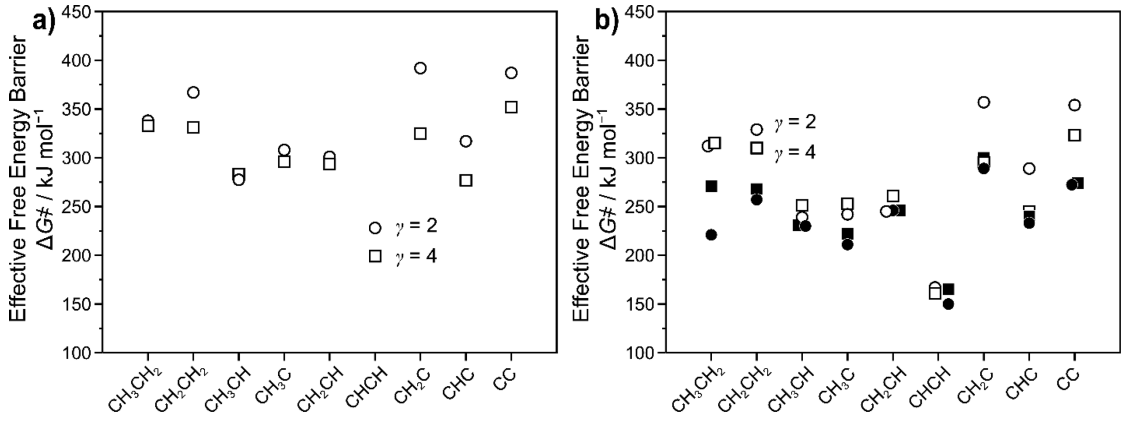

Figure 9. Effective free energy $\Delta G^{\ddagger}$ (eq 10) barriers for C−C bond cleavage in ethane-derived intermediates at $\gamma = 2$ (○) and $\gamma = 4$ (□) on (a) Ir(111) surface and (b) Ir_{119} particle. Filled data points indicate C−C bond activation near corners and edges on Ir_{119}. Transition state structures are shown in the Supporting Information (SI, Figures S6−S9).

(196−199 kJ mol^{-1}) and λ (4) values on this surface model are much larger than those measured on 0.7 nm Ir ($\Delta G^{\ddagger}$ = 156 ± 5 kJ mol^{-1}; λ = 3.0 ± 0.2)[44] and on 7 nm Ir (130 ± 5 kJ mol^{-1}; 3.3 ± 0.2).[45] This surface model fails to reflect observed trends because C−C hydrogenolysis is a reaction with a positive activation area ($\Delta A^{\ddagger}$ = 0.059 nm^2 at γ = 2), and these periodic surface models prevent the H* adlayer from relaxing laterally, causing excessive H*-coverage effects.

The Ir_{119} nanoparticle model, in contrast, has under-coordinated corner and edge atoms which allow the H* adlayer to relax because of the curvature of the metal surface. For reactions taking place on the (111) terrace sites on the Ir_{119} particle, $\Delta G^{\ddagger}$ decreases from 188 kJ mol^{-1} at γ = 0 to 167 kJ mol^{-1} at γ = 2 then decreases weakly to 161 kJ mol^{-1} at γ = 4 before it increases rapidly with the removal of additional H* atoms (Figure 6). Similarly, the highest DFT predicted turnover rates are at γ = 1−3 (~7 × 10^{-6} s^{-1}, 10 bar H_2) despite the slight decrease in $\Delta G^{\ddagger}$ at γ = 4 because of the impact of H_2 pressure. These results for Ir_{119} indicate that *CH−CH* bond cleavage would likely require an average of 2 vacant sites on the terrace (γ = 2) which gives a λ value of 3, in a better agreement with the measured values on small 0.7 nm Ir clusters (156 ± 5 kJ mol^{-1}; 3.0 ± 0.2).[44]

CH−CH bond cleavage occurs preferentially near corners and edges on the Ir_{119} particle compared to terrace sites (Figure 8). For example, ΔG_k for *CH−CH* bond cleavage at γ = 2 on a corner site is 24 kJ mol^{-1} lower than that on the (111) terrace. ΔG_k on the corner and edge sites decreases from 184 kJ mol^{-1} at γ = 0 to 122 kJ mol^{-1} at γ = 2 (slope of − 31 kJ mol^{-1} γ^{-1}) before it decreases weakly to 97 kJ mol^{-1} at γ = 19 (slope of − 1 kJ mol^{-1} γ^{-1}) (Figure 4). The minimum effective free energy barrier $\Delta G^{\ddagger}$ is observed at γ = 2 (147 kJ mol^{-1}) on a corner site (Figure 6) that gives the maximum turnover rate of ~ 7 × 10^{-4} s^{-1} at 10 bar H_2 (Figure 7). These results indicate that the adlayer relaxation becomes more evident near the edges of the particle at high coverages. Next, we examine C−C bond cleavage in the other ethane-derived intermediates and compare the DFT-predicted turnover rates with the measured data.

4.4. C−C Bond Cleavage in Other Ethane-Derived Intermediates. The relative contribution of C−C bond rupture in each of the C_2H_{6-y} intermediates (where $0 \le y \le 6$) to hydrogenolysis turnover rate depends on their respective $\Delta G^{\ddagger}$ values (eq 9). $\Delta G^{\ddagger}$ values for C−C bond cleavage in all dehydrogenated species are shown in Figure 9 for both the H*-covered Ir(111) surface and Ir_{119} particle on two and four vacancies. Transition-state structures are shown in the Supporting Information (SI, Figures S6−S9). Similar to *CH−CH* bond cleavage, C−C bond cleavage in nearly all other intermediates occurs preferentially on four vacancies (γ = 4) on the Ir(111) surface (Figure 9a). C−C bond cleavage on the (111) terrace of the Ir_{119} particle exhibits similar trends but the two-vacancy activations become comparable or slightly more favorable than four-vacancy activations in some intermediates (Figure 9b). Corner and edge sites, however, can cleave the C−C bond in all intermediates on two vacancies with lower $\Delta G^{\ddagger}$ values than four-vacancy activations. C−C cleavage via the *CHCH* intermediate has significantly lower $\Delta G^{\ddagger}$ values than all other intermediates, consistent with previous findings for ethane[45] and larger *n*-alkanes[49] (RC*C*R′) on a bare Ir(111) surface. For example, the DFT-predicted turnover rate calculated using eq 9 for *CH−CH* bond cleavage on the terrace of Ir_{119} particle at γ = 2 (8.2 × 10^{-7} s^{-1}) is 5 orders of magnitude higher than that for the next most reactive intermediate CH_3CH (6.5 × 10^{-12} s^{-1}) (593 K, 0.2 bar C_2H_6, and 18 bar H_2). These findings indicate that C−C bond cleavage in the other intermediates is unlikely to contribute to the measured hydrogenolysis rate.

The sum of DFT-predicted rates for C−C bond cleavage in the *CHCH* intermediate, at all configurations of H*, and for all values of γ is shown in Figure 9 as a function of H_2 pressure (5−20 bar H_2). For the Ir(111) surface, the turnover rate decreases from 4.3 × 10^{-8} to 1.5 × 10^{-10} s^{-1} with a H_2-pressure dependence of $[H_2]^{-4}$ (i.e., λ = 4). These rates are far lower than the measured rates and do not agree with experimentally measured H_2 pressure inhibition. DFT-predicted rates on an Ir_{119} particle are much higher than on an Ir(111) surface and show a H_2-pressure dependence of $[H_2]^{-3}$, consistent with the measured rates and λ on 0.7 nm Ir[44] and on 7 nm Ir[45] clusters (Figure 10). However, measured turnover rates increase with increasing particle size and with slight increase in λ value, in disagreement with the particle size effect predicted by DFT where corner and edge sites exhibit higher reactivity than terrace sites. The increase in measured turnover rates with increasing particle size suggests that low-coordinated metal atoms could be more saturated with H* than in our model (H* can also strongly bind to the bridging sites on the edges of Ir particles as shown in a previous DFT study)[81] or poisoned with CH_{0-3} products, rendering them less active than terrace sites. Despite this discrepancy in predicting particle size effects, this study shows

DOI: 10.1021/acscatal.8b01114
ACS Catal. 2018, 8, 6375−6387

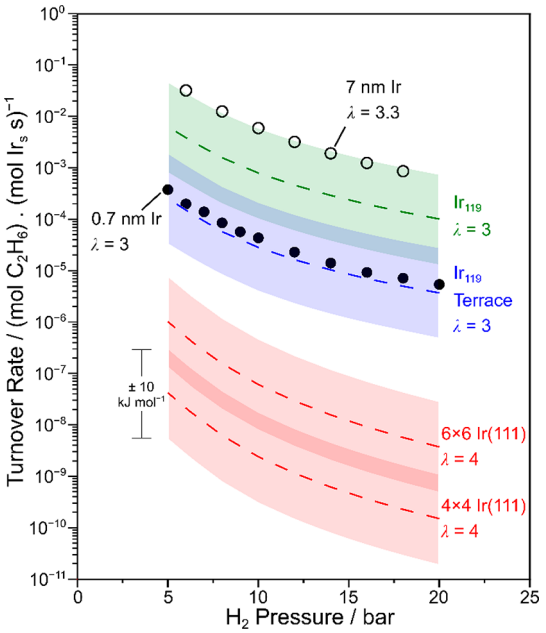

Figure 10. DFT-predicted hydrogenolysis rates (eq 9) (dashed lines) on Ir(111) surface (red), Ir_{119} particle (green) and on terrace sites of Ir_{119} particle (blue) compared to measured rates on 0.7 nm Ir[44] (●) and 7 nm Ir[45] (○) as a function of H_2 pressure (593 K, 0.2 bar C_3H_6). Shadings represent the effect of ± 10 kJ mol^{-1} difference in calculated $\Delta G^{\ddagger}$ on predicted turnover rates.

that metal particle models can describe reactions at high coverages more accurately than flat periodic surfaces.

5. CONCLUSIONS

Ethane hydrogenolysis was used as a probe reaction to demonstrate the rigorous estimation of site requirements using ab initio methods, expose artifacts associated with modeling reactions at high coverage on single-crystal catalyst models, and show how these artifacts are eliminated using hemispherical nanoparticle models. Free energy barriers to cleave the C−C bond in ethane-derived intermediates were calculated by DFT on H*-covered Ir(111) surfaces and Ir_{119} particles, and these results show that transition states on periodic surface models communicate through coadsorbate interactions at high coverages, presenting significant artifacts. Coadsorbed H* atoms destabilize C−C bond activation, reflecting the inadequacy of Langmuirian models in describing reactions in dense adlayers. Instead, reactions at high surface coverages must be treated as nonideal systems in which reaction rates depend on their activation areas; positive activation area reactions induce strain in the surrounding adlayer while negative activation area reactions relieve strain. The Ir_{119} particle permits lateral relaxation of the H* adlayer, unlike the Ir(111) surface model, allowing C−C bond activation to occur at a lower number of vacancies and with activation barriers consistent with the measured values. Calculated effective free energy barriers ($\Delta G^{\ddagger}$) and DFT-predicted turnover rates on Ir_{119} particle confirm that C−C bond activation in ethane occurs predominantly via the *CHCH* intermediate with two H* atoms displaced from the surface, consistent with prior studies and H_2-pressure kinetic dependencies. This study focuses on a relatively simple and extensively studied reaction to provide compelling fundamental insights into how one can accurately model complex reactions occurring on curved surfaces at high coverages that prevail in practical catalysis.

■ ASSOCIATED CONTENT

Supporting Information

The Supporting Information is available free of charge on the ACS Publications website at DOI: 10.1021/acscatal.8b01114.

Details of DFT calculations and transition states structures (PDF)

■ AUTHOR INFORMATION

Corresponding Author

*E-mail: hibbitts@che.ufl.edu.

ORCID

David Hibbitts: 0000-0001-8606-7000

Notes

The authors declare no competing financial interest.

■ ACKNOWLEDGMENTS

D.H. acknowledges Profs. David Flaherty (University of Illinois, Urbana−Champaign) and Enrique Iglesia (University of California, Berkeley) for helpful discussions. A.A. acknowledges Saudi Arabian Cultural Mission (SACM) and King Faisal University, Saudi Arabia, for funding his graduate studies and research. Computational resources were provided by University of Florida Research Computing. This work also used the Extreme Science and Engineering Discovery Environment (XSEDE; CTS160041), which is supported by National Science Foundation Grant No. ACI-1548562. Manuscript reviews and proofreading from Alexander Hoffman (University of Florida) and Pavlo Kravchenko (University of Florida) are gratefully acknowledged.

■ REFERENCES

(1) García-Diéguez, M.; Iglesia, E. Structure sensitivity via decoration of low-coordination exposed metal atoms: CO oxidation catalysis on Pt clusters. *J. Catal.* **2013**, *301*, 198−209.

(2) Dobrin, S. CO oxidation on Pt nanoclusters, size and coverage effects: a density functional theory study. *Phys. Chem. Chem. Phys.* **2012**, *14*, 12122−12129.

(3) Boudart, M.; Djéga-Mariadassou, G. *Kinetics of heterogeneous catalytic reactions*; Princeton University Press, 2014.

(4) Araya, P.; Porod, W.; Sant, R.; Wolf, E. E. Monte carlo simulations of carbon monoxide oxidation on Pt catalysts. *Surf. Sci.* **1989**, *208*, L80−L90.

(5) Chin, Y.-H. C.; Buda, C.; Neurock, M.; Iglesia, E. Reactivity of chemisorbed oxygen atoms and their catalytic consequences during CH_4-O_2 catalysis on supported Pt clusters. *J. Am. Chem. Soc.* **2011**, *133*, 15958−15978.

(6) Getman, R. B.; Schneider, W. F.; Smeltz, A. D.; Delgass, W. N.; Ribeiro, F. H. Oxygen-coverage effects on molecular dissociations at a Pt metal surface. *Phys. Rev. Lett.* **2009**, *102*, 076101.

(7) Gürbüz, E. I.; Hibbitts, D. D.; Iglesia, E. Kinetic and mechanistic assessment of alkanol/alkanal decarbonylation and deoxygenation pathways on metal catalysts. *J. Am. Chem. Soc.* **2015**, *137*, 11984−11995.

(8) Lausche, A. C.; Medford, A. J.; Khan, T. S.; Xu, Y.; Bligaard, T.; Abild-Pedersen, F.; Nørskov, J. K.; Studt, F. On the effect of coverage-dependent adsorbate−adsorbate interactions for CO methanation on transition metal surfaces. *J. Catal.* **2013**, *307*, 275−282.

(9) Getman, R. B.; Schneider, W. F. DFT-based characterization of the multiple adsorption modes of nitrogen oxides on Pt(111). *J. Phys. Chem. C* **2007**, *111*, 389−397.

(10) Getman, R. B.; Schneider, W. F. DFT-based coverage-dependent model of Pt-catalyzed NO oxidation. *ChemCatChem* **2010**, *2*, 1450−1460.

DOI: 10.1021/acscatal.8b01114
ACS Catal. 2018, 8, 6375−6387

(11) Smeltz, A. D.; Getman, R. B.; Schneider, W. F.; Ribeiro, F. H. Coupled theoretical and experimental analysis of surface coverage effects in Pt-catalyzed NO and O_2 reaction to NO_2 on Pt(111). *Catal. Today* **2008**, *136*, 84−92.
(12) Getman, R. B.; Xu, Y.; Schneider, W. F. Thermodynamics of environment-dependent oxygen chemisorption on Pt(111). *J. Phys. Chem. C* **2008**, *112*, 9559−9572.
(13) Langmuir, I. The mechanism of the catalytic action of platinum in the reactions $2CO+O_2=2CO_2$ and $2H_2+O_2=2H_2O$. *Trans. Faraday Soc.* **1922**, *17*, 621.
(14) Djéga-Mariadassou, G.; Boudart, M. Classical kinetics of catalytic reactions. *J. Catal.* **2003**, *216*, 89−97.
(15) Berlowitz, P. J.; Peden, C. H. F.; Goodman, D. Kinetics of carbon monoxide oxidation on single-crystal palladium, platinum, and iridium. W. *J. Phys. Chem.* **1988**, *92*, 5213−5221.
(16) Allian, A. D.; Takanabe, K.; Fujdala, K. L.; Hao, X.; Truex, T. J.; Cai, J.; Buda, C.; Neurock, M.; Iglesia, E. Chemisorption of CO and mechanism of CO oxidation on supported platinum nanoclusters. *J. Am. Chem. Soc.* **2011**, *133*, 4498−4517.
(17) Hibbitts, D. D.; Dybeck, E.; Lawlor, T.; Neurock, M.; Iglesia, E. Preferential activation of CO near hydrocarbon chains during Fischer−Tropsch synthesis on Ru. *J. Catal.* **2016**, *337*, 91−101.
(18) Liu, J.; Hibbitts, D.; Iglesia, E. Dense CO adlayers as enablers of CO hydrogenation turnovers on Ru surfaces. *J. Am. Chem. Soc.* **2017**, *139*, 11789−11802.
(19) Loveless, B. T.; Buda, C.; Neurock, M.; Iglesia, E. CO chemisorption and dissociation at high coverages during CO hydrogenation on Ru catalysts. *J. Am. Chem. Soc.* **2013**, *135*, 6107−6121.
(20) Deshlahra, P.; Conway, J.; Wolf, E. E.; Schneider, W. F. Influence of dipole-dipole interactions on coverage-dependent adsorption: CO and NO on Pt(111). *Langmuir* **2012**, *28*, 8408−8417.
(21) Schmidt, D. J.; Chen, W.; Wolverton, C.; Schneider, W. F. Performance of cluster expansions of coverage-dependent adsorption of atomic oxygen on Pt(111). *J. Chem. Theory Comput.* **2012**, *8*, 264−273.
(22) Xu, Z.; Kitchin, J. R. Probing the coverage dependence of site and adsorbate configurational correlations on (111) surfaces of late transition metals. *J. Phys. Chem. C* **2014**, *118*, 25597−25602.
(23) İnoğlu, N.; Kitchin, J. R. Simple model explaining and predicting coverage-dependent atomic adsorption energies on transition metal surfaces. *Phys. Rev. B: Condens. Matter Mater. Phys.* **2010**, *82*, 045414.
(24) Greeley, J.; Mavrikakis, M. A first-principles study of surface and subsurface H on and in Ni(111): diffusional properties and coverage-dependent behavior. *Surf. Sci.* **2003**, *540*, 215−229.
(25) Shetty, S.; Jansen, A. P. J.; van Santen, R. A. Direct versus hydrogen-assisted CO dissociation. *J. Am. Chem. Soc.* **2009**, *131*, 12874−12875.
(26) Lanzani, G.; Nasibulin, A. G.; Laasonen, K.; Kauppinen, E. I. CO dissociation and CO+O reactions on a nanosized iron cluster. *Nano Res.* **2009**, *2*, 660−670.
(27) Greeley, J.; Mavrikakis, M. A first-principles study of methanol decomposition on Pt(111). *J. Am. Chem. Soc.* **2002**, *124*, 7193−7201.
(28) Greeley, J.; Mavrikakis, M. Competitive paths for methanol decomposition on Pt(111). *J. Am. Chem. Soc.* **2004**, *126*, 3910−3919.
(29) Tritsaris, G. A.; Greeley, J.; Rossmeisl, J.; Nørskov, J. K. Atomic-scale modeling of particle size effects for the oxygen reduction reaction on Pt. *Catal. Lett.* **2011**, *141*, 909−913.
(30) Avanesian, T.; Dai, S.; Kale, M. J.; Graham, G. W.; Pan, X.; Christopher, P. Quantitative and atomic-scale view of CO-induced Pt nanoparticle surface reconstruction at saturation coverage via DFT calculations coupled with in situ TEM and IR. *J. Am. Chem. Soc.* **2017**, *139*, 4551−4558.
(31) Nolte, P.; Stierle, A.; Jin-Phillipp, N. Y.; Kasper, N.; Schulli, T. U.; Dosch, H. Shape changes of supported Rh nanoparticles during oxidation and reduction cycles. *Science* **2008**, *321*, 1654−1658.
(32) Eren, B.; Zherebetskyy, D.; Patera, L. L.; Wu, C. H.; Bluhm, H.; Africh, C.; Wang, L.-W.; Somorjai, G. A.; Salmeron, M. Activation of Cu(111) surface by decomposition into nanoclusters driven by CO adsorption. *Science* **2016**, *351*, 475−478.
(33) Weitkamp, J.; Jacobs, P. A.; Martens, J. A. Isomerization and hydrocracking of C_9 through C_{16} n-alkanes on Pt/HZSM-5 zeolite. *Appl. Catal.* **1983**, *8*, 123−141.
(34) McVicker, G.; Daage, M.; Touvelle, M. S.; Hudson, C. W.; Klein, D. P.; Baird, W. C., Jr; Cook, B. R.; Chen, J. G.; Hantzer, S.; Vaughan, D. W.; Ellis, E. S.; Freeley, O. C. Selective ring opening of naphthenic molecules. *J. Catal.* **2002**, *210*, 137−148.
(35) Do, P.; Alvarez, W.; Resasco, D. Ring opening of 1,2- and 1,3-dimethylcyclohexane on iridium catalysts. *J. Catal.* **2006**, *238*, 477−488.
(36) Shi, H.; Gutiérrez, O. Y.; Haller, G. L.; Mei, D.; Rousseau, R.; Lercher, J. A. Structure sensitivity of hydrogenolytic cleavage of endocyclic and exocyclic C−C bonds in methylcyclohexane over supported iridium particles. *J. Catal.* **2013**, *297*, 70−78.
(37) Shi, H.; Li, X.; Haller, G. L.; Gutiérrez, O. Y.; Lercher, J. A. Active sites and reactive intermediates in the hydrogenolytic cleavage of C−C bonds in cyclohexane over supported iridium. *J. Catal.* **2012**, *295*, 133−145.
(38) Weisang, F.; Gault, F. G. Selective isomerization of methylpentanes on iridium catalysts. *J. Chem. Soc., Chem. Commun.* **1979**, *11*, 519−520.
(39) Speight, J. G. *Petroleum Refinery Processes*; John Wiley and Sons, Inc.: New York, 2012; pp 1−49.
(40) Iglesia, E.; Reyes, S. C.; Madon, R. J.; Soled, S. L. Selectivity control and catalyst design in the Fischer−Tropsch synthesis: sites, pellets, and reactors. In *Advances in Catalysis*; Academic Press, 1993; Vol. *39*, pp 221−302.
(41) Bond, G. C. *Metal-Catalysed Reactions of Hydrocarbons*; Springer: New York, 2005.
(42) Cimino, A.; Boudart, M.; Taylor, H. Ethane hydrogenation-cracking on iron catalysts with and without alkali. *J. Phys. Chem.* **1954**, *58*, 796−800.
(43) Morikawa, K.; Benedict, W. S.; Taylor, H. S. The activation of specific bonds in complex molecules at catalytic surfaces. II. The carbon-hydrogen and carbon-carbon bonds in ethane and ethane-d. *J. Am. Chem. Soc.* **1936**, *58*, 1795−1800.
(44) Flaherty, D. W.; Iglesia, E. Transition-state enthalpy and entropy effects on reactivity and selectivity in hydrogenolysis of n-alkanes. *J. Am. Chem. Soc.* **2013**, *135*, 18586−18599.
(45) Flaherty, D. W.; Hibbitts, D. D.; Gürbüz, E. I.; Iglesia, E. Theoretical and kinetic assessment of the mechanism of ethane hydrogenolysis on metal surfaces saturated with chemisorbed hydrogen. *J. Catal.* **2014**, *311*, 350−356.
(46) Cortright, R. D.; Watwe, R. M.; Spiewak, B. E.; Dumesic, J. A. Kinetics of ethane hydrogenolysis over supported platinum catalysts. *Catal. Today* **1999**, *53*, 395−406.
(47) Cortright, R. D.; Watwe, R. M.; Dumesic, J. A. Ethane hydrogenolysis over platinum. *J. Mol. Catal. A: Chem.* **2000**, *163*, 91−103.
(48) Sinfelt, J. Catalytic hydrogenolysis of ethane over the noble metals of group VIII. *J. Catal.* **1967**, *8*, 82−90.
(49) Hibbitts, D. D.; Flaherty, D. W.; Iglesia, E. Effects of chain length on the mechanism and rates of metal-catalyzed hydrogenolysis of n-alkanes. *J. Phys. Chem. C* **2016**, *120*, 8125−8138.
(50) Engstrom, J. R.; Goodman, D. W.; Weinberg, W. H. Hydrogenolysis of ethane, propane, n-butane, and neopentane on the (111) and (110)-(1 × 2) surfaces of iridium. *J. Am. Chem. Soc.* **1988**, *110*, 8305−8319.
(51) Bond, G. C.; Cunningham, R. H. Alkane transformations on supported platinum catalysts. *J. Catal.* **1997**, *166*, 172−185.
(52) Bond, G. C.; Slaa, J. C. Catalytic and structural properties of ruthenium bimetallic catalysts: effects of pretreatment on the behaviour of various $RuAl_2O_3$ catalysts in alkane hydrogenolysis. *J. Mol. Catal. A: Chem.* **1995**, *101*, 243−253.
(53) Flaherty, D. W.; Hibbitts, D. D.; Iglesia, E. Metal-catalyzed C-C bond cleavage in alkanes: effects of methyl substitution on transition-state structures and stability. *J. Am. Chem. Soc.* **2014**, *136*, 9664−9676.

DOI: 10.1021/acscatal.8b01114
ACS Catal. 2018, 8, 6375−6387

(54) Hibbitts, D. D.; Flaherty, D. W.; Iglesia, E. Role of branching on the rate and mechanism of C−C cleavage in alkanes on metal surfaces. *ACS Catal.* **2016**, *6*, 469−482.
(55) Boudart, M.; Ptak, L. D. Reactions of neopentane on transition metals. *J. Catal.* **1970**, *16*, 90−96.
(56) Flaherty, D. W.; Uzun, A.; Iglesia, E. Catalytic ring opening of cycloalkanes on Ir clusters: alkyl substitution effects on the structure and stability of C−C bond cleavage transition states. *J. Phys. Chem. C* **2015**, *119*, 2597−2613.
(57) Hibbitts, D. D.; Jiménez, R.; Yoshimura, M.; Weiss, B.; Iglesia, E. Catalytic NO activation and NO−H_2 reaction pathways. *J. Catal.* **2014**, *319*, 95−109.
(58) Hecker, W. Reduction of NO by H_2 over silica-supported rhodium: infrared and kinetic studies. *J. Catal.* **1985**, *92*, 247−259.
(59) Behtash, S.; Lu, J.; Williams, C. T.; Monnier, J. R.; Heyden, A. Effect of palladium surface structure on the hydrodeoxygenation of propanoic acid: identification of active sites. *J. Phys. Chem. C* **2015**, *119*, 1928−1942.
(60) Shangguan, J.; Olarte, M. V.; Chin, Y.-H. (Cathy). Mechanistic insights on C-O and C-C bond activation and hydrogen insertion during acetic acid hydrogenation catalyzed by ruthenium clusters in aqueous medium. *J. Catal.* **2016**, *340*, 107−121.
(61) Witzke, M. E.; Almithn, A. S.; Coonrod, C. L.; Hibbitts, D. D.; Flaherty, D. W. Mechanisms and active sites for C−O bond rupture within 2-methyltetrahydrofuran over nickel phosphide catalysts. *J. Catal.* **2018**.
(62) Kua, J.; Faglioni, F.; Goddard, W. A. Thermochemistry for Hydrocarbon Intermediates Chemisorbed on Metal Surfaces: $CH_{n-m}(CH_3)_m$ with n = 1, 2, 3 and m ≤ n on Pt, Ir, Os, Pd, Rh, and Ru. *J. Am. Chem. Soc.* **2000**, *122*, 2309−2321.
(63) Chorkendorff, I.; Niemantsverdriet, J. W. *Concepts of modern catalysis and kinetics*; Wiley-VCH Verlag: Weinheim, 2006.
(64) Kemball, C.; Taylor, H. S. The catalytic decomposition of ethane and ethane—hydrogen mixtures. *J. Am. Chem. Soc.* **1948**, *70*, 345−351.
(65) Sinfelt, J. H.; Taylor, W. F.; Yates, D. J. C. Catalysis over supported metals. III. Comparison of metals of known surface area for ethane hydrogenolysis. *J. Phys. Chem.* **1965**, *69*, 95−101.
(66) Watwe, R. M.; Cortright, R. D.; Nørskov, J. K.; Dumesic, J. Theoretical studies of stability and reactivity of C_2 hydrocarbon species on pt clusters, pt(111), and pt(211). A. *J. Phys. Chem. B* **2000**, *104*, 2299−2310.
(67) Zhao, Z.-J.; Moskaleva, L. V.; Rösch, N. Ring-opening reactions of methylcyclopentane over metal catalysts, M = Pt, Rh, Ir, and Pd: a mechanistic study from first-principles calculations. *ACS Catal.* **2013**, *3*, 196−205.
(68) Kresse, G.; Furthmüller, J. Efficiency of ab-initio total energy calculations for metals and semiconductors using a plane-wave basis set. *Comput. Mater. Sci.* **1996**, *6*, 15−50.
(69) Kresse, G.; Furthmüller, J. Efficient iterative schemes for *ab initio* total-energy calculations using a plane-wave basis set. *Phys. Rev. B: Condens. Matter Mater. Phys.* **1996**, *54*, 11169−11186.
(70) Kresse, G.; Hafner, J. Ab initio molecular-dynamics simulation of the liquid-metal-amorphous-semiconductor transition in germanium. *Phys. Rev. B: Condens. Matter Mater. Phys.* **1994**, *49*, 14251−14269.
(71) Kresse, G.; Hafner, J. *Ab initio* molecular dynamics for liquid metals. *Phys. Rev. B: Condens. Matter Mater. Phys.* **1993**, *47*, 558−561.
(72) Blöchl, P. E. Projector augmented-wave method. *Phys. Rev. B: Condens. Matter Mater. Phys.* **1994**, *50*, 17953−17979.
(73) Kresse, G.; Joubert, D. From ultrasoft pseudopotentials to the projector augmented-wave method. *Phys. Rev. B: Condens. Matter Mater. Phys.* **1999**, *59*, 1758−1775.
(74) Hammer, B.; Hansen, L. B.; Nørskov, J. K. Improved adsorption energetics within density-functional theory using revised Perdew-Burke-Ernzerhof functionals. *Phys. Rev. B: Condens. Matter Mater. Phys.* **1999**, *59*, 7413−7421.
(75) Pack, J. D.; Monkhorst, H. J. Special points for Brillouin-zone integrations—a reply. *Phys. Rev. B* **1977**, *16*, 1748−1749.
(76) Krekelberg, W. P.; Greeley, J.; Mavrikakis, M. Atomic and molecular adsorption on Ir(111). *J. Phys. Chem. B* **2004**, *108*, 987−994.
(77) Olsen, R. A.; Kroes, G. J.; Baerends, E. J. Atomic and molecular hydrogen interacting with Pt(111). *J. Chem. Phys.* **1999**, *111*, 11155−11163.
(78) Christmann, K.; Ertl, G.; Pignet, T. Adsorption of hydrogen on a Pt(111) surface. *Surf. Sci.* **1976**, *54*, 365−392.
(79) Christmann, K. Interaction of hydrogen with solid surfaces. *Surf. Sci. Rep.* **1988**, *9*, 1−163.
(80) Spenadel, L.; Boudart, M. Dispersion of platinum on supported catalysts. *J. Phys. Chem.* **1960**, *64*, 204−207.
(81) Almithn, A. S.; Hibbitts, D. D. Supra-monolayer coverages on small metal clusters and their effects on H_2 chemisorption particle size estimates. *AIChE J.* **2018**, DOI: 10.1002/aic.16110.
(82) Henkelman, G.; Jónsson, H. Improved tangent estimate in the nudged elastic band method for finding minimum energy paths and saddle points. *J. Chem. Phys.* **2000**, *113*, 9978−9985.
(83) Jónsson, H.; Mills, G.; Jacobsen, K. W. Nudged elastic band method for finding minimum energy paths of transitions. In *Classical and Quantum Dynamics in Condensed Phase Simulations*; Berne, B. J., Ciccotti, G., Coker, D. F., Eds.; World Scientific, 1998; pp 385−404.
(84) Henkelman, G.; Jónsson, H. A dimer method for finding saddle points on high dimensional potential surfaces using only first derivatives. *J. Chem. Phys.* **1999**, *111*, 7010−7022.
(85) Mcvicker, G.; Baker, R. K.; Garten, R. L.; Kugler, E. L. Chemisorption properties of iridium on alumina catalysts. *J. Catal.* **1980**, *65*, 207−220.
(86) Kip, B. J.; Duivenvoorden, F. B. M.; Koningsberger, D. C.; Prins, R. Determination of metal particle size of highly dispersed rhodium, iridium and platinum catalysts by hydrogen chemisorption and EXAFS. *J. Am. Chem. Soc.* **1986**, *108*, 5633−5634.
(87) Sen, B.; Vannice, M. A. The influence of platinum crystallite size on H_2 and CO heats of adsorption and CO hydrogenation. *J. Catal.* **1991**, *130*, 9−20.
(88) Brooks, C. S. Characterization of iridium catalyst surfaces by gas chemisorption. *J. Colloid Interface Sci.* **1970**, *34*, 419−427.
(89) Wellendorff, J.; Silbaugh, T. L.; Garcia-Pintos, D.; Nørskov, J. K.; Bligaard, T.; Studt, F.; Campbell, C. T. A benchmark database for adsorption bond energies to transition metal surfaces and comparison to selected DFT functionals. *Surf. Sci.* **2015**, *640*, 36−44.
(90) Campbell, C. T.; Sellers, J. R. V. The entropies of adsorbed molecules. *J. Am. Chem. Soc.* **2012**, *134*, 18109−18115.
(91) Acharya, C. K.; Turner, C. H. CO oxidation with Pt(111) supported on pure and boron-doped carbon: a DFT investigation. *Surf. Sci.* **2008**, *602*, 3595−3602.
(92) Davda, R. R.; Alcalá, R.; Shabaker, J.; Huber, G.; Cortright, R. D.; Mavrikakis, M.; Dumesic, J. A. 11 DFT and experimental studies of C-C and C-O bond cleavage in ethanol and ethylene glycol on Pt catalysts. In *Studies in surface science and catalysis*; Anpo, M., Onaka, M., Yamashita, H., Eds.; Elsevier, 2003; Vol. *145*, pp 79−84.
(93) Jelic, J.; Meyer, R. J. Density functional theory examination of Pd(111) and Pd(100) under NO oxidation conditions. *Phys. Rev. B: Condens. Matter Mater. Phys.* **2009**, *79*, 125410.
(94) Greeley, J.; Rossmeisl, J.; Hellmann, A.; Norskov, J. K. Theoretical trends in particle size effects for the oxygen reduction reaction. *Z. Phys. Chem.* **2007**, *221*, 1209−1220.
(95) Bondi, A. Van der Waals Volumes and Radii. *J. Phys. Chem.* **1964**, *68*, 441−451.
(96) Zefirov, Y. V.; Zorkii, P. M. Van der Waals radii and their application in chemistry. *Russ. Chem. Rev.* **1989**, *58*, 421−440.
(97) Batsanov, S. S. Van der Waals radii of elements. *Inorg. Mater.* **2001**, *37*, 871−885.
(98) Rowland, R. S.; Taylor, R. Intermolecular nonbonded contact distances in organic crystal structures: Comparison with distances expected from van der Waals radii. *J. Phys. Chem.* **1996**, *100*, 7384−7391.

DOI: 10.1021/acscatal.8b01114
ACS Catal. 2018, 8, 6375−6387